Experimental and Numerical Characterization of an Ejector Pump Burner for Small Scale Firing Systems

Muhammad Ferdous Raiyan
muhammad.ferdous.raiyan@tecnico.ulisboa.pt

Instituto Superior Técnico, Universidade de Lisboa, Portugal

November 2019

Abstract

The present work aims to develop an air entrainment model for ejector pump burner where fuel jet draws ambient air for a premixed combustion which is mainly used in domestic cooking stove. A detailed numerical and experimental parametric study has been performed to understand air entrainment model thus determining the key factors directly affecting the amount of air entrainment which consequently affects the equivalence ratio (ϕ). Based on CFD modeling, the effects of tube diameter (D), injector geometry, injection condition, distance between tube and injector (Δ) have been studied which are also characterized by non-intrusive diagnostic techniques. An optimum limit regarding tube size (D) and distance (Δ) have been proposed after parametric study.

Ideal and *real* geometries in CFD environment have been studied to investigate their influence on primary aeration. *Real* geometry leads to higher entrainment and the results showed close matching with PIV technique with a 3% to 6% discrepancy. While comparing to ideal case, the discrepancy remained in between 15% to 20%. Similar behavior in terms of discrepancy were obtained while evaluating equivalence ratio (ϕ) for different test cases (CFD) and comparing them to the results from spectroscopy. The primary aeration characteristics based on isothermal and non-isothermal modeling have been investigated and isothermal model predicted more aeration than non-isothermal case. A simple premixed combustion model with ideal geometry estimated the heat release and the distribution of mass fraction of different species. Temperature of an experimental case is measured with thermocouple and temperature from same model developed from CFD is compared. Effects of different parameters on equivalence ratio and CO emission have been explored from the results.

Keywords: Ejector pump burner, Air entrainment, Combustion, Numerical modeling, PIV, Spectroscopy

1. Introduction

Combustion can be defined as the mechanism in which the chemical energy of fuel is converted into thermal energy. Most of the combustion processes require at least two components in the reactants, which are: a fuel and an oxidant. Rearrangements of the chemical bonds in these compounds lead to the formation of "products". Three very important parameters: temperature, reactants mixing and time have strong influence on combustion [1].

Estimated three billion people around the world burn firewood, coal, dung, crop residue and charcoal in traditional stoves for cooking and heating purpose [2]. Household air pollution due to incomplete combustion of such fuels is responsible around the world for 4.3 million premature deaths per year and 1.7 million of them is in South Asia. It surpasses the burden of disease from any other energy related environmental risk factor [3]. While modeling an ejector pump burner small scale firing system, most important things are to develop a proper air entrainment system for mixing purpose that will provide not only a suitable temperature but also a clean burning to reduce environmental emissions, as well as to optimize the geometry of tube and injector, and studying different fuel injection conditions. The fuel jet drags the surrounding air through the entrainment and subsequently gets mixed in the mixing tube and this primary air entrainment is controlled by momentum transfer from fuel jet to surrounding air before the combustion takes place. Thus amount of fuel supplied as well as flow rate are extremely crucial to study the air entrainment model.

Singh et al. [4] developed a finite element model (FEM) in order to predict the amount of primary air entrainment. The results were to be compared with the theoretical ones from [5]. It was observed that the numerical results were near to the theoretical ones, as primary air entrainment becomes higher

for a higher density of fuel gas. The aspect ratio (ratio of tube and injector diameters) and density ratio were found to be the key factors influencing entrainment and mixing. They are also responsible for causing instability in jet as well as recirculation in the mixing tube. It was also observed that Reynolds number has a negligible effect on entrainment ratio. Later an experimental study [6] was performed for the same purpose and then compared again with the results from [5]. The result showed that measured amount of primary air entrained was higher for a higher ratio of burner port to injector orifice diameter. In the experiment [6], entrainment ratio increases to a maximum value as the jet location is taken away from the tube inlet. For the configurations investigated, enhancement up to 30 percent has been noticed in the entrainment ratio with shift in jet location. For a smaller tube diameter and jet located at the inlet of the tube, the circular jet entrains more air than non-circular jets. When the length of tube increases or shifted jet locations, the non-circular jets entrain more of ambient fluid. Among the various non-circular geometries taken for investigation, the jet having the cross section of an isosceles triangle causes maximum entrainment.

Computational fluid dynamics (CFD) modeling can give important insights regarding steady state flow, combustion and heat transfer characteristics in a burner [7]. After design modifications based on results from three dimensional (3D) CFD modeling, the proposed burner showed a 2.5 % of increased thermal efficiency for liquefied petroleum gas (LPG) fired burner and 10 % for pipeline natural gas (PNG) fired burner. The CFD model didn't simulate the exact experimental setup and that's why improvement in percentage efficiency was compared between model predictions and experiments rather than taking absolute values into account.

CFD tools can also be helpful to optimize the firing system by taking into consideration the changes geometrical parameters injectors, such as diameter and exit position. Zhao et al. [8] observed that the natural gas-air mixing process inside the mixing chamber shows that methane concentration uniformity increases with the increase of distance from injector exit. It was found that injector outlet position at -3.0 mm enhances the overall performance of premixed cylindrical burner, and also when the injector diameter is not less than 1.6 mm. Emission characteristics of NOx and CO were examined experimentally.

One of the key things while performing different investigations regarding development of premixed burners where air entrainment plays a very important role, is to lower the emission of NOx. Controlling the operating parameters e.g. velocity of fuel and air injections along with fuel temperature and the temperature of pre-heated air control the emission of NOx significantly [9]. Moreover, reducing temperature of the charge, there is an increase in excess air ratio, which allows a considerable decrease in NOx emission and the concentration is kept within international standards [10]. Also, advantage of premixed combustion has been found also in literature as it notably decreases the NOx emission as no fuel NOx and prompt NOx are produced.

2. Numerical Modeling

CFD is a virtual prototyping tool that guides to build precision flow models by solving different transport equations. The combustion flow features can be analyzed in detail with CFD. Temperature, mixing of different species, flow velocity, concentration and flame stability, and concentration of combustion species can be computed for different types of model geometries with high level of accuracy [11]. The chemical and physical phenomena of the reacting flow may be simulated by solving a generalized set of conservation equations numerically which includes the equation for conservation of mass, momentum (Navier Stokes equations) and energy. Additional equations are required for modeling turbulence and combustion. The fundamental approach for numerical simulation of the governing equations is the finite element or finite difference approximations.

2.1. Modeling Framework for Turbulent Combustion

he following instantaneous governing equations presented are for a reacting flow, which are in nonconservative and compressible form for the mass density, momentum, species mass fractions and internal energy [12]. Continuity:

$$\frac{\partial \rho}{\partial t} + \nabla \cdot \rho \mathbf{u} = 0 \qquad (1)$$

Momentum:

$$\rho \frac{D\mathbf{u}}{Dt} = \rho \frac{\partial \mathbf{u}}{\partial t} + \rho(\mathbf{u} \cdot \nabla)\mathbf{u} = -\nabla p + \nabla \cdot \tau + \rho \sum_{k=1}^{N} Y_k \mathbf{f}_k \qquad (2)$$

Species continuity ($k=1,...,N$):

$$\rho \frac{DY_k}{Dt} = \rho \frac{\partial Y_k}{\partial t} + \rho \mathbf{u} \cdot \nabla Y_k = \nabla \cdot (-\rho \mathbf{V}_k Y_k) + \omega_k \quad (3)$$

Energy:

$$\rho \frac{De}{Dt} = \rho \frac{\partial e}{\partial t} + \rho \mathbf{u} \cdot \nabla e = -\nabla \cdot \mathbf{q} - p \nabla \cdot \mathbf{u} + \tau : \nabla \mathbf{u} +$$

$$\rho \sum_{k=1}^{N} Y_k \mathbf{f}_k \cdot \mathbf{V}_k$$

$$\text{(4)}$$

2.2. Geometry Design

Figure 1 is the schematic 2D diagram of the firing system comprised of the injector and the mixing tube. The original tube has a length of 10.1 cm with an external diameter of 1.5 cm as well as 0.25 cm of thickness. The material is stainless steel with a straight inlet and outlet shape. The symbols L and D respectively represent the height of the tube and the external diameter whereas d and l denote the diameter of the injector and height respectively. The mixing tube has a small wall thickness t and the distance between tube and injector has been denoted by Δ.
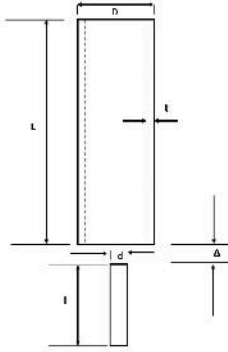
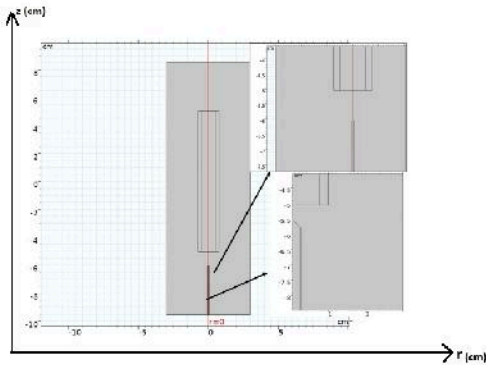Figure 1: 2D sketch of tube and ideal injector.

Figure 2: Design in COMSOL modeler.

Figure 2 depicts the 2D axisymmetric design in the modeling environment. The axes z and r define the axis coordinate system in the design environment. Throughout the work, axis z will stand for the vertical coordinate system and axis r will represent horizontal coordinate system that is the radial distance from the center line.

2.3. Grid generation

In Figure 3, the mesh generated for the computational model has been represented in two parts (upper and lower). Figure 3(a) is the view of meshing done for fuel injection and the entrance of fuel and entrained air through the bottom of the tube whereas Figure 3(b) depicts the meshing for the tube exit to the surrounding. The total number of elements has been set around 189k after the grid independence test. Figure 3(c) shows the variation of entrainment ratio with different grid settings. Significant variations have been observed while the cell numbers varied in between 5000 to 50000. Later with more refinement, results were also found to be changing and near 189000 elements, they exhibited steady behavior with very little change in the output results. Later, for further observation, the grid number was increased to almost 0.4 million but only 0.2% change was noticed. So, considering the computational cost, it was concluded to keep the grid settings corresponding to 189000 cells.

(a) Mesh lower part   (b) Mesh upper part
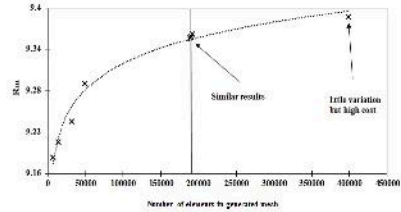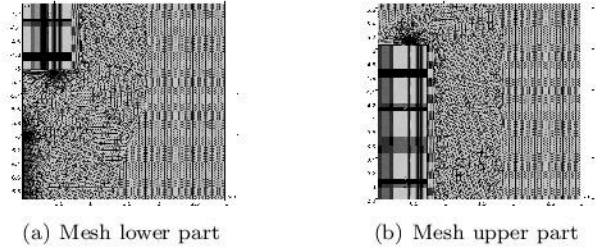
(c) Grid independence test

Figure 3: Grid generation and grid indepence test for the ejector pump system.

2.4. Selection of physics and boundary condition

After developing the 2D geometry and setting up the appropriate grid, suitable physics needed to be selected in order to carry out the computational study. In this method, the flow has been considered as turbulent as well as the mixing process in the tube. Due to the presence and reaction of chemical species and considering both isothermal and non-isothermal condition, the features namely: *Turbulent Flow k-ω, Transport of Concentrated Species, Heat Transfer in Fluids, Reacting Flow* and *Non-*

isothermal Flow. For each physics, it's extremely important to choose the exact boundary conditions and other necessary governing features and parameters.

After setting up all the necessary boundary conditions corresponding to respective physics, the model has been prepared for executing the computation by running the solver. The stationary study steps are used when field variables do not change over time, such as in stationary problems and also to find the solution to linear and nonlinear stationary problems (also called static or steady-state problems).

3. Experimental Setup and Instrumentation

he basic setup of the experiment is simple and requires less supporting equipment. A schematic of the general experimental setup (without spectroscopy and PIV) used in this work is presented in Figure 4. In order to ensure safe and proper flow of fuel to the system, the main propane intake has been taken through a computer controlled flow meter which is operated by the *Alicat* developed *Flow Vision* software. The flow meter used here has a capacity of passing 5 SLPM flow through it with ±0.4% accuracy. Using this general setup, blowoff and flashback limit for the particular tube and two different injectors have been determined. These limits have been used later in the experimental setup using PIV and spectroscopy.
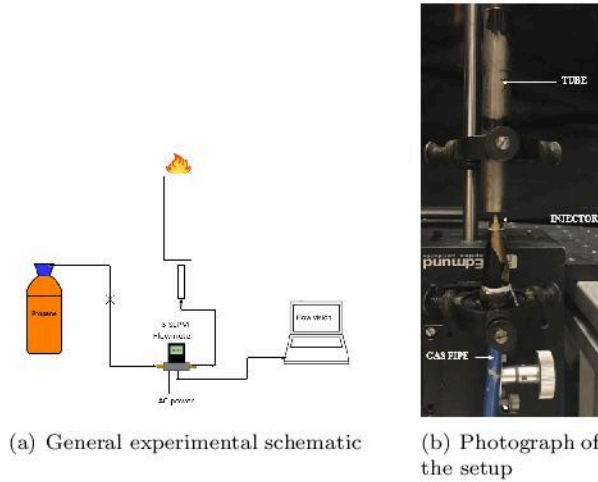

(a) General experimental schematic

(b) Photograph of the setup

Figure 4: Schematic diagram and photograph of experimental setup.

3.1. Chemiluminescence Spectroscopy

The radical chemiluminescence emissions of OH^*, CH^* and C_2^* can be considered as 'finger prints' for flame diagnostics [13], specially CH^* and C_2^*, corresponding to blue and green colors in visible spectrum. The fundamental of this process is based on the spontaneous emission of electromagnetic radiation from the chemical species during the combustion process. The emitted radiation will have an intensity as well as wavelength as the excited radical is formed during reaction and goes to its ground state. The wavelength and intensity can be correlated to different flame properties uniquely based on the setup [14]. The main purpose of this diagnostic technique in this experiment is to estimate the equivalence ratio (ϕ) depending on the peak values of intensities from the emission of respective chemical radical which are OH^*, CH^* and C_2^*. The ratio of these radicals are taken subsequently. The observed narrow band peaks are presented in Figure 5 and the complete schematic is shown in Figure 6.
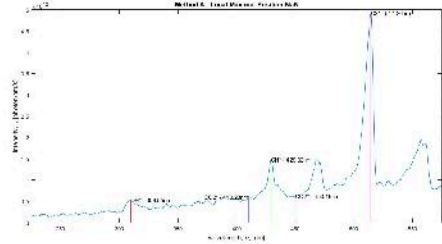

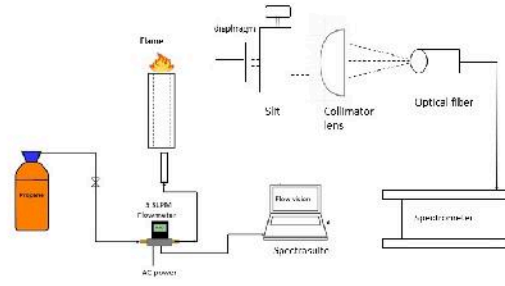Figure 5: Emission spectrum during experiment.

Figure 6: Spectroscopy schematic.

Using the data obtained from *SpectraSuite* while performing chemiluminescence spectroscopy, a *MATLAB* routing has been used to process the data and based on the ratios of the radicals OH^*, CH^* and C_2^* obtained throughout the whole equivalence ratio, calibration curves are formed which are presented in Figure 7. The relationships established from the calibration curves can be expressed as:

$$\phi = 0.4271 \left(\frac{OH^*}{CH^*}\right)^{-0.702} \tag{5}$$

$$\phi = 0.750 \left(\frac{OH^*}{C_2^*}\right)^{-0.21} \tag{6}$$

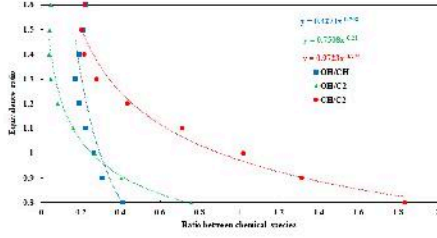$$\phi = 0.9723 \left(\frac{CH^*}{C_2^*}\right)^{-0.274} \tag{7}$$

4

Figure 7: Calibration curves for equivalence ratio range.

The curve representing Equation 7 has been chosen as it has a higher inclination or slope. Otherwise, if the curve is too vertical or too horizontal, the ratios between chemical species don't allow to accurately predict the equivalence ratio.

3.2. Particle Image Velocimetry

Particle Image Velocimetry (PIV) is a quantitative velocity measuring technique. The PIV technique can be classified into two steps, visualization and image analysis. The flow is seeded with tracing particles (paraffin oil) and illuminated by a double pulsed laser in the area of investigation to produce a green light planar sheet which has a of 530 nm. The double pulsed laser is synchronized with a high speed CCD camera using a synchronizer which is connected to the primary acquisition system. The camera captures two consecutive frames of laser lighted particles seeded in the flow. After that, the 2D velocity field can be determined by making cross correlation of the two consecutive frames as well as the time interval between laser pulses and the distance traveled by the seeding particles.
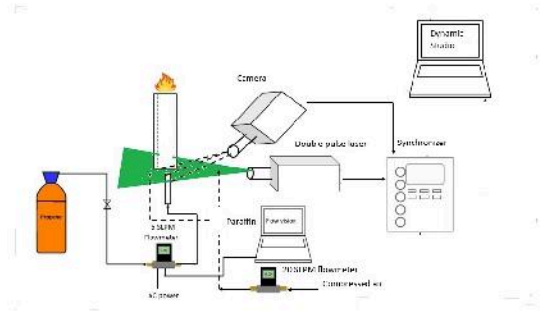

Figure 8: Schematic of PIV setup.

The schematic diagram of PIV setup is depicted in Figure 8 and the photograph in Figure 9. Compressed air has been used to force the paraffin oil from a venturi like reservoir and controlled by an *Alicat* 20 SLPM flowmeter operated by *Flow Vision* software. The green region in the diagram represents the laser sheet covering the area of interest which is the air entrainment zone and the surrounding places near the entrainment zone are seeded with the paraffin particles. As a result, the air entrained is illuminated due to the presence of the seeding particles and the instantaneous positions are captured by the high resolution camera.
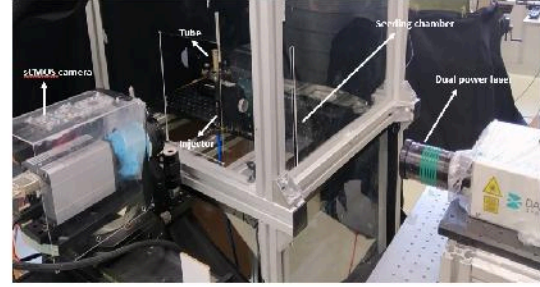

Figure 9: Schematic of PIV setup.

4. Results and Discussions

4.1. Influence of Injector Geometry and Diameter

The geometry of the injector plays an important role on the amount of air entrained and thus affecting the equivalence ratio. Depending on the injector geometry, it is expected to observe variation in entrainment ratio. In this work, two different injector geometries have been used, namely *ideal* and *real* as shown in Figure 10.

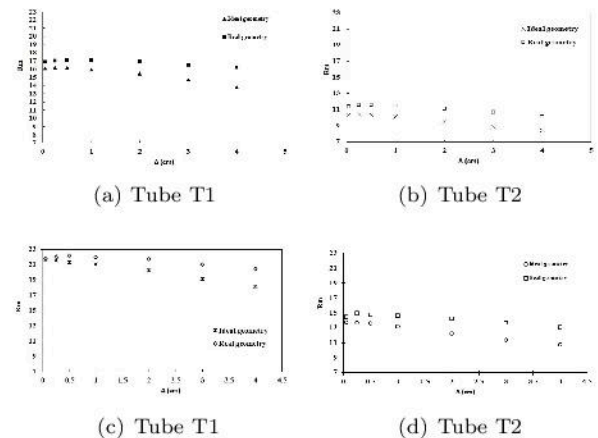Figure 10: Ideal (left) and real (right) injector geometry.

(a) Tube T1　　　　(b) Tube T2

(c) Tube T1　　　　(d) Tube T2

Figure 11: Distribution of entrainment ratio for tubes T1 and T2 with d1(a) and d2(b) injector for distance Δ=0.05 to 4cm with ideal and real geometries at v_{in}=1.88 SLPM.

Figure 11 shows the entrainment ratio (Rm) changing with distance for both tubes and injectors. With increase in distance, Rm is also decreasing. For the same injection condition in terms of mass flow rate, injector d2 has exhibited higher entrainment ratio. Using tube T1 also shows superiority over tube T2 considering entrainment ratio. With distance ($\Delta = 0.05$ to 2cm), the discrepancy between ideal and real injector was limited within 12% but with bigger distance, it reaches upto 20%. Also Figure 12 describes the reason for the discrepancy between ideal and real geometry as due to the velocity profile shape for real geometry in Figure 12(b), higher momemntum transfer allows it to drag more air than the shape observed in Figure 12(a).
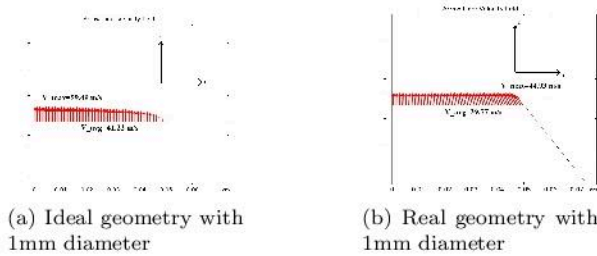

(a) Ideal geometry with 1mm diameter

(b) Real geometry with 1mm diameter

Figure 12: Velocity vector distribution over the top surface of 1mm injector for ideal (a) and real(b) geometries at $\dot{v}_{in}$=1.88 SLPM.

4.2. Influence of distance between injector and tube on primary aeration

In order to investigate the effect of distance between and mixing tube and injector, three tubes and two injectors have been selected. The injectors are d1 and d2 used previously and an additional tube (T3) with external diameter of 1.2 cm has been chosen. For all six cases, the inlet boundary condition remained same. Considering the computational cost, seven different distances have been selected which are 0.05cm, 0.25cm, 0.5cm, 1cm, 2cm, 3cm and 4cm. For the same injection condition i.e. same in-
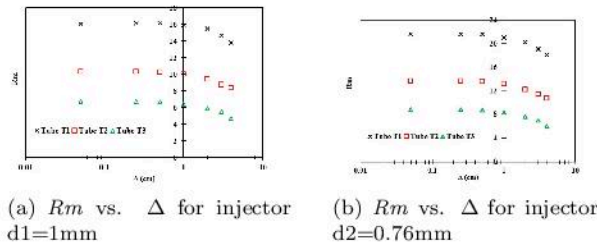

(a) Rm vs. Δ for injector d1=1mm

(b) Rm vs. Δ for injector d2=0.76mm

Figure 13: Descension of entrainment ratio from Δ= 0.25cm to Δ=4cm using ideal injectors d1 and d2

let boundary condition and injection diameter (d1) in Figure 13(a), tube T1 has more amount of air entrained than tubes T2 and T3. But as the dis-

tance increased, the entrainment performance also decreased. For the first four distances which range from 0.05cm to 1cm, the change wasn't significant as the deviation of entrainment from each consecutive distance didn't vary more than 2%. But for bigger distances, such as: 2cm to 4cm, there was a swift decline in the entrainment ratio and the change is almost 15% for tube T1 with distance 4cm, whereas for T2 and T3, it was around 5%. Similar behavior was also observed in Figure 13(b).

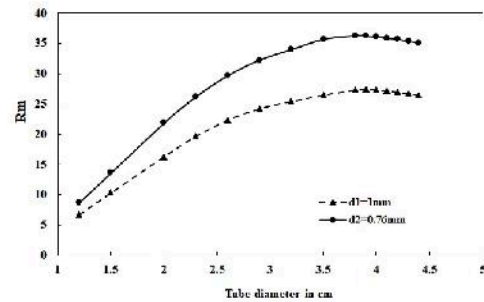### 4.3. Effect of mixing tube diameter on air entrainment

Figure 14: Effect of tube diameter on air entrainment.

It is observed from Figure 14 that for all cases, air entrainment found to be higher for the injector d2 than that of d1. As the diameter of the tube was further increased and varied between 2.3cm to 3.8cm, the difference between each consecutive cases became lower and ranged between 17% to 0.4%. Beyond 3.8cm diameter, the change was steady and the similar behavior was also found while investigating with injector d2. Almeida et al. [15] also reported the similar phenomena regarding a certain limit of increasing the tube diameter.

4.4. Combustion Modeling in CFD Environment

In all cases, the ideal injector geometry has been used along with tube T2 made of stainless steel. The combustion model presented here has been developed by using one step propane combustion mechanism. Later two cases considering two step mechanism will be given to observe CO emission and equivalence ratio.

4.4.1 Consistency in the behavior of combustion model entrainment ratio

$$C_3H_8 + 5O_2 \longrightarrow 3CO_2 + 4H_2O \qquad (8)$$

Figure 15 gives the decreasing trend of entrained air mass flow as the distance (Δ) increases. As expected, which is observed from previous studies, injector d2 gives more amount of entrained air for same inlet mass flow rate condition. In an average, amount of air entrained with d2 was found to be

30% higher than injector d1. Also, fall in mass flow rate value is around 3% for lower distances such as 0.25cm and 0.5cm. With increase in distance, the difference becomes bigger and reaches approximately 6% to 8%.
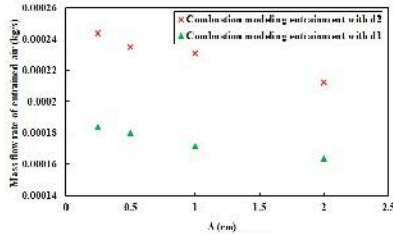

Figure 15: Variation in combustion model entrained air mass flow rate for injector d1 and d2 for distances Δ=0.25cm to 2cm.

4.4.2 Effect of hot test and cold test on primary aeration

It can be observed from Figure 16 that there's a significant difference in terms of primary aeration while performing the computational investigation in hot flow test and cold flow test. In almost all cases, 14% more primary aeration has been achieved during the cold test. The preheating effect caused by combustion is responsible for lower primary air entrainment. During the hot test, due to rise in temperature of the burner, the temperature of the fuel air mixture flowing through the mixing tube increases, thus leading to lower density and higher velocity. In an investigation on a self aspirating burner, Namkhat and Jugjai [16] observed the effect of changes in the combustion air temperature on the primary aeration. It was also found that the level of primary aeration decreased with an increasing preheated air temperature.
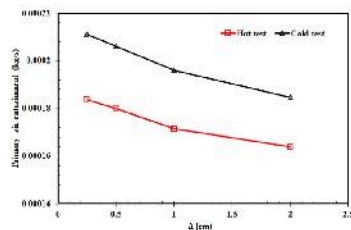

Figure 16: Discrepancy and trend of primary air entrainment during hot test and cold test.

4.4.3 Estimation of equivalence ratio for d1 and d2 with increase in Δ

It is evident from Figure 17 that equivalence ratio is strongly influenced by the size of the injector as well as the distance between mixing tube and injector. Using a bigger diameter injector (d1), gives less amount of primary aeration when compared to the primary aeration caused by smaller injector (d2). From parametric study, it was found that with the increase in distance, entrainment ratio decreases and as a result, the equivalence ratio also rises, taking the flame towards rich or more rich condition. Due to the injector diameter difference, a discrepancy level of approximately 30% was observed between the equivalence ratio obtained from two cases.
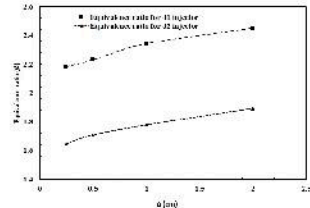

Figure 17: Evolution in equivalence ratio for two injectors d1 and d2 with variation in distance from Δ=0.25cm to 2cm.

4.4.4 Temperature and mass fraction distribution

(a) Temperature development contour of flame

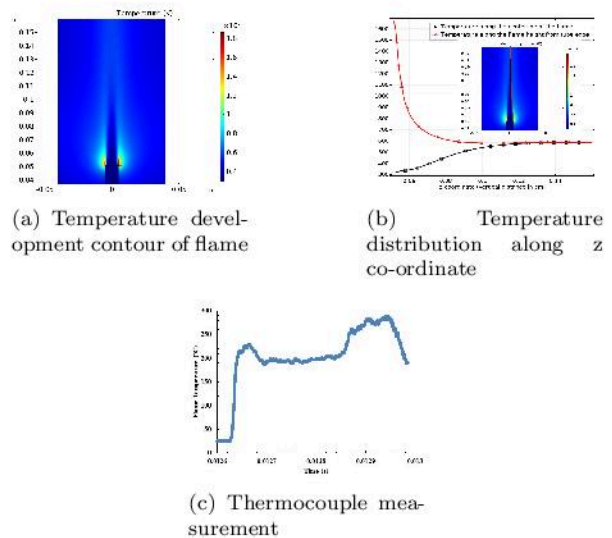(b) Temperature distribution along z co-ordinate

(c) Thermocouple measurement

Figure 18: Temperature profile(a,b) from CFD and data acquired by thermocouple in *QuickDAQ* environment(c) for an inlet condition of 0.806SLPM, injector d1, tube T2 and Δ=0.5cm.

The surrounding area around the inner flame structure at the reaction zone exhibited the highest temperature as soon as the ignition occurs. As the flame is developed in a conical shape shown in Figure 18(a), the temperature along the core also

7

increases whereas the flame temperature along vertical direction from the mixing tube edge gradually decreases. Trends of temperature are plotted in Figure 18(b) with the data obtained from CFD environment. The flame height was nearly 12 cm in experiment and similar flame structure has also been observed from the numerical modeling. The temperature of the flame at a height of 5 cm from the tube surface was measured as 565K (Figure 18(c)) whereas the numerical modeling shows around 530K in the same position.

4.4.5 Mass fraction distribution

(a) Mass fraction of C_3H_8

(b) Mass fraction of O_2

(c) Mass fraction of CO_2

(d) Mass fraction of H_2O

(e) Mass fraction of CO, Δ=0.5cm
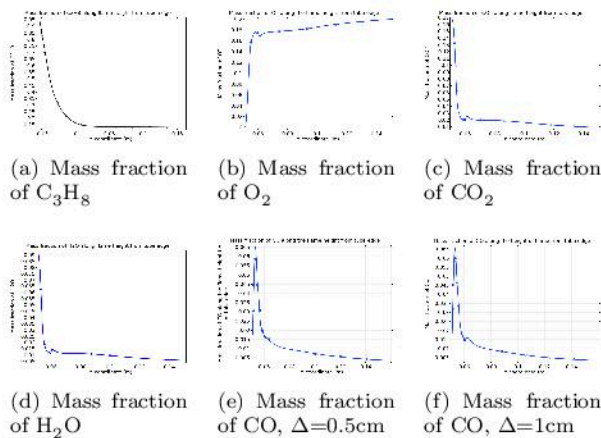
(f) Mass fraction of CO, Δ=1cm

Figure 19: Mass fraction of different chemical species for an inlet condition of 0.806SLPM, injector d1, tube T2.

Figure 19(a) shows the depletion of C_3H_8 from the injection towards combustion. At the position of 0.05m from CFD modeler interface, the combustion starts at the top of tube surface. Subsequently, the amount of C_3H_8 was lowered as the flame is developed. For O_2, the mass fraction was considered in the surrounding air as 0.23. At the beginning of combustion the O_2 present in the fuel air mixture was depleted. But later with the flame development, more O_2 from surround air joined and thus the mass fraction almost becomes equal to the original amount in the ambient air which is depicted in Figure 19(b). For the products of combustion CO_2 and H_2O, presented in Figure 19(c) and Figure 19(d) the initial mass fractions from the reaction zone start to decrease along the flame height. Both of them experience a slight jump as the exit the reaction zone in the modeling environment as they are joined by surrounding air's molecule containing little amount of H_2O and CO_2. Entrainment ratio which is a function of primary air entrainment, decreases when the distance (Δ) increases. Figure 19(e), which is a setup with Δ=0.5cm that causes more aeration, shows that the amount of CO starts

to increase in the first stage of combustion as it stayed just below 0.065. With the supply of more air, it starts to decrease as combustion continues to occur. But for a distance of Δ=1cm, presented in Figure 19(f), the value of CO slightly goes above 0.065 as the case has now moved to more rich condition with the increase of equivalence ratio.

4.5. Analysis of Results from Chemiluminescence Spectroscopy

Several conditions have been tested and the equivalence ratios are evaluated from the obtained results. Different injection mass flow rates have been set for three different tubes working with the injector d2. The mass flow rates varied for all the tubes as they were selected based on the stability limit (flashback and blow-off) of flames uniquely identified for each tube. The three tubes are named as T4, T5 and T6. Using the relationship from Equation 7, the equivalence ratio is calculated. It was decided to investigate three tubes with a fixed injector by using three different injection conditions. It must be mentioned that the injector position was maintained almost at the entrance of the tube. Figure 20 shows the be-
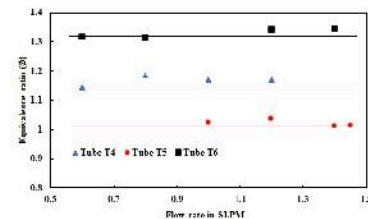

Figure 20: Equivalence ratio obtained from spectroscopy for different tubes.

havior of the equivalence ratio for three different tubes operating under different injection conditions in terms of mass flow rate but the injector diameter remains same. For all three cases, it's clearly visible that there's no significant variation in equivalence ratio even though the mass flow rate of the fuel has been changing for a fixed injector position.

4.6. Analysis of Results from Particle Image Velocimetry

The raw PIV data for each test case was imported in the form of .csv file which has been processed by *MATLAB* script in order to obtain the mass flow rate of air entrainment as well as the profile. Just below the bottom line of the tube, the coordinates from the captured frame are detected and based on that, the data have been filtered by excluding those which are not of interest. A radial coordinate system is developed to define the position of each velocity vector and to perform the surface integration in order to calculate the mass flow rate of entrainment.

The surface integral formula for the mass flow rate is:

$$\dot{m} = \iint \rho \vec{V} \cdot d\vec{A} = \int_0^{2\pi} \int_0^R V_a r \, dr \, d\theta \qquad (9)$$

(a) Velocity vector for Δ=0.5cm

(b) Entrainment profile for Δ=0.5cm

(c) Velocity vector for Δ=1cm

(d) Entrainment profile for Δ=1cm

(e) Velocity vector for Δ=2cm

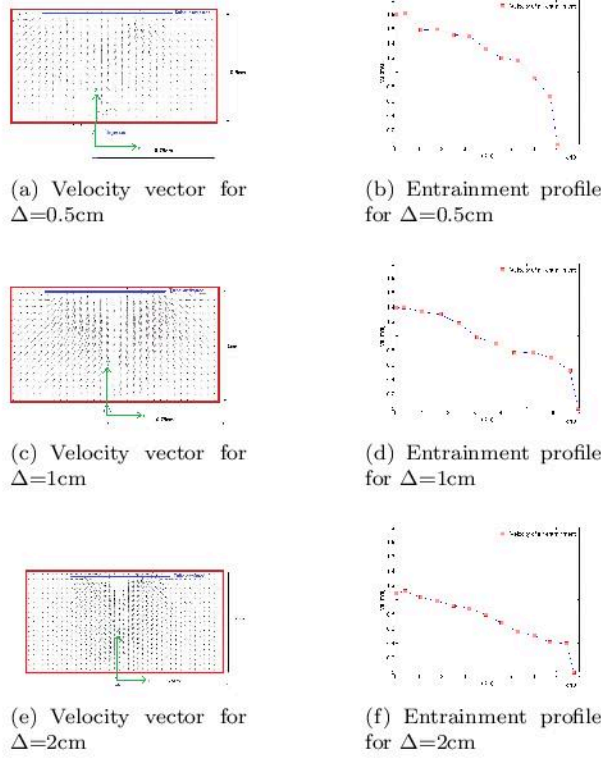(f) Entrainment profile for Δ=2cm

Figure 21: Velocity vector and development of air entrainment profile.

4.7. Discrepancy in entrainment ratio using air-air approach from PIV setup and CFD design (real and ideal)
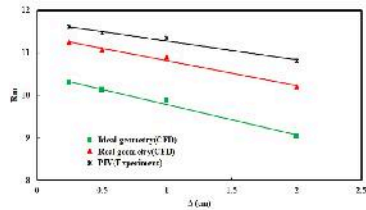

Figure 22: Observation of entrainment ratio discrepancy between values from CFD environment (ideal and real injector) and PIV with real injector.

The difference between results from PIV and ideal geometry started with a discrepancy level of 12% when Δ=0.25cm which is depicted in Figure 22. As the distance increases, the error level grows bigger and for a distance of Δ=2cm, the difference

was found almost 19%. While using the real injector design, the PIV shows a close matching with the numerical results. For Δ=0.25cm and 0.5cm, it accounted for only 3.5% of error. With the increase in distance, the error level rises slightly but it was limited within 6.5%.

4.8. Comparison of ϕ from CFD and spectroscopy

From Figure 23, it is observed that CFD modeling with ideal geometry also shows the similar behavior for the equivalence ratio. As the injection flow rate increases, the equivalence ratio differed from each other only at a level of 2% to 3%. The level of discrepancy between CFD values (ideal) and spectroscopy values varied in between 14% to 18%. As discussed before, modeling with real injector geometry would provide values of equivalence ratio closer to the spectroscopy value. The CFD results were improved with real geometry and the level of discrepancy fell down below 10% when comparing to the spectroscopy results.
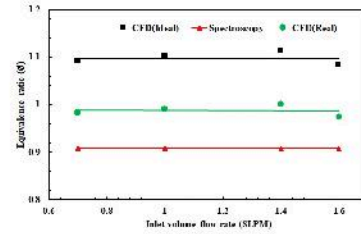

Figure 23: Validation of CFD model by observing discrepancy with equivalence ratio values obtained from spectroscopy.
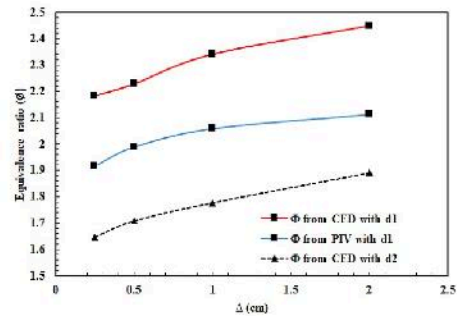
4.9. Comparison of ϕ from CFD and PIV

Figure 24: Graphical representation of the equivalence ratio derived from CFD and PIV for tube T2, injector d1 and Δ=0.25cm, 0.5cm, 1cm and 2cm.

Figure 24 depicts the trend of equivalence ratio with the increase in distance between tube and the injector, for both CFD and PIV technique. Proportional relationship has been observed between the distance (Δ) and equivalence ratio (ϕ). The difference between the equivalence ratio obtained

from shows an initial discrepancy level of 8% for 0.25cm distance between CFD and PIV. With the increase in distance, the error level increased and for Δ=2cm distance, 15.86% difference has been found. Nonetheless, the CFD results can be improved and error level can be reduced significantly by performing the computation with real injector geometry.

5. Conclusions

Parametric study has been performed in order to understand the operation and working principle of ejector pump burner. Close relationship has been observed for tube diameter, injector geometry and distance between tube and injector influencing the entrainment ratio. Two geometries named as ideal and real are investigated in CFD environment and compared with the results from PIV and spectroscopy analysis. Results show close matching while comparing CFD real geometry and experimental output. The discrepancy level varies in between 15% to 20% for ideal and experimental comparison whereas it was lowered to 5% to 10% for real geometry. Separately, CFD combustion model also validate the behavior of air entrainment and equivalence ratio with change in different parameters. Diagnostic techniques results also prove that the aforementioned parameters play crucial role in the air entrainment model. Finally it was intended to provide guidelines based on CFD and experimental findings to design simple, easy functioning, cheap and less emission domestic cooking stove. For any firing system, the proper oxidization of fuel plays the most important role and thus this work primary suggested different approaches for the development of an air entrainment model.

References

[1] DE Winterbone and A Turan. Advanced thermodynamics for engineers. *Butterworth-Heinmann*, ISBN:9780080999838, 2015.

[2] WHO. Fuel for life: household energy and health. *World Health Organization*, 2006.

[3] S Bonjour. Solid fuel use for household cooking: country and regional estimates for 1980–2010. *Environmental health perspectives*, 121(7):784–790, 2013.

[4] G Singh, T Sundararajan, and USP Shet. Entrainment and mixing studies for a variable density confined jet. *Numerical Heat Transfer, Part A: Applications*, 35(2):205–223, 1999.

[5] R Pritchard, JJ Guya, and NE Connor. Handbook of industrial gas utilization:engineering principles and practice. *New York: Van Nostrand Reinhold Co.*, ISBN-13: 978-0442266356, 1977.

[6] G Singh, T Sundararajan, and KA Bhaskaran. Mixing and entrainment characteristics of circular and noncircular confined jets. *Journal of Fluids Engineering*, 125:835–842, 2003.

[7] P Boggavarapu, B Ray, and RV Ravikrishna. Thermal efficiency of lpg and png-fired burners: Experimental and numerical studies. *Fuel*, 116:709–715, 2014.

[8] DF Zhao, FG Liu, XY You, R Zhang, BL Zhang, and GL He. Optimization of a premixed cylindrical burner for low pollutant emission. *Energy Conversion and Management*, 99:151–160, 2015.

[9] Z Wei, X Li, L Xu, and Tan C. Optimization of operating parameters for low nox emission in high- temperature air combustion. *Energy Fuels*, 26(5):2821–2829, 2012.

[10] U Kesgin. Study on prediction of the effects of design and operating parameters on nox emissions form a lean burn natural gas engine. *Energy Conversion and Management*, 44(4):907–921, 2003.

[11] AA Boateng. Rotary kilns:transport phenomena and transport processes. *Butterworth-Heinemann*, ISBN: 9780080557120, 2008.

[12] T Echekki and E Mastorakos. Turbulent combustion modeling: Advances, new trends and perspectives. *Springer*, ISBN:978-94-007-0412-1, 2011.

[13] AG Gaydon and HG Wolfhard. Flames, their structure, radiation, and temperature. *Springer US*, 978-1-5041-2585-7, 1960.

[14] T Trindade, A Ferreira, and EC Fernandes. Characterization of combustion chemiluminescence: an image processing approach. *Procedia Technology*, 17:194–201, 2014.

[15] ALMS Almeida, RM Laranjeira, LMP Monteiro, AD Santos, and EC Fernandes. 1d model for a low nox ejector-pump like burner. *Experimental Thermal and Fluid Science*, 100:171–192, 2019.

[16] A Namkhat and S Jugjai. Primary air entrainment characteristics for a self-aspirating burner: Model and experiments. *Energy*, 35:1701–1708, 2010.